The Investigation of Effect of Defects on the Structural, Optical, and Magnetic Properties of $CuAlO_2$

C. Boyraz[a], A. Guler[b], Ö. Karataş[c,d,*], P. Aksu[e], M. Can Alphan[f] and L. Arda[f]

[a] *Department of Mechanical Engineering, Marmara University, 34840, Istanbul, Turkey*
[b] *Department of Electrical and Electronics Engineering, Marmara University, 34840, Istanbul, Turkey*
[c] *Department of Electric and Energy, Konya Technical University, 42250, Konya, Turkey*
[d] *Department of Physics, Gebze Technical University, 41400, Kocaeli, Turkey*
[e] *Institute of Nanotechnology, Gebze Technical University, 41400, Kocaeli, Turkey*
[f] *Department of Mechatronic Engineering, Bahcesehir University, 34349 Istanbul, Turkey*

Received: 17.02.2022 & Accepted: 02.09.2022

Doi: 10.12693/APhysPolA.142.464 *e-mail: okaratas@ktun.edu.tr

Rapid synthesis of delafossite $CuAlO_2$ was achieved by a solid-state reaction method. The synthesized sample was subjected to phase analysis by X-ray diffraction. The desired crystalline phase was obtained and all peaks in the X-ray diffraction phase investigation were found to belong to the $CuAlO_2$ pattern. Morphological and stoichiometric properties were defined by a scanning electron microscope and in-situ attachment of energy dispersive spectroscopy. X-ray photoelectron spectroscopy measurements were done to provide a detailed elemental composition analysis in the parts per thousand ranges. X-ray photoelectron spectroscopy measurements revealed that the core level of the 4 electron species Cu 2*p*, Al 2*p*, and O 1*s* exists. The structural defects of $CuAlO_2$ were investigated using the Agilent Cary Eclipse Fluorescence Spectrophotometer. The photoluminescence measurements showed that the near-band emission, cooper vacancy, and oxygen vacancy emission occurred. The nature of optical and magnetic properties of the $CuAlO_2$ sample was defined by Quantum Design Physical Properties Measurement System and correlated with the X-ray photoelectron spectroscopy and photoluminescence results.

topics: delafossite $CuAlO_2$, optical and magnetic properties, solid-state reaction method, nanostructures

1. Introduction

The demand for developing new or alternative materials for existing technology is an everlasting desire and effort in research areas. For this purpose, providing maximal efficiency and suitability at a reasonable costs and uncompromised safety plays a crucial role in the development of new functional nanodevices. Transparent conductive oxides (TCO) with their direct applications are gaining considerable technological interest and potential usage, especially in solar cells and their related components such as touch panels and transparent electrodes in flat panel displays [1]. In addition to these purposes of usage, a potential interest in its thermoelectric properties has been achieved nowadays [2]. As p-type conductivity (with relatively high hole mobility), TCOs act as active devices for industrial applications [3, 4]. $CuAlO_2$ has a rhombohedral type of crystal structure in which Al^{3+} ions are coordinated by six O^{2-} ions as octahedral packing, and Cu^{2+} ions are linearly coordinated by two O^{2-} ions. The distances corresponding to the Cu–O and Al–O bonds are 1.861 and 1.912 Å, respectively. In the literature, even though there are many studies on the growth, electrical, and optical characterization of $CuAlO_2$, the basics of $CuAlO_2$ still need to be clarified [5–18].

In wide bandgap semiconductors, defects play a critical role in their structural, optical properties, and electrical conduction. When we consider n-type ZnO materials with intrinsic defects, oxygen vacancy and interstitial zinc are the primary sources of structural, optical properties, and electrical conduction [19–22].

In intrinsic p-type TCO semiconductors, the conduction mechanism is similar to that of n-type TCO semiconductors. For p-type $CuAlO_2$ materials, some intrinsic defects such as Cu vacancy, Al vacancy, and interstitial oxygen may contribute to their structural, optical, and electrical conduction properties.

In order to improve the structural, optical properties and electrical conduction of materials, attention should be paid to defects due to annealing temperature, annealing time, and additive elements, as these are some of the most critical parameters in determining the desired physical properties. Depending on the synthesizing technique, bulk and powder forms of $CuAlO_2$ have varying annealing temperatures and durations. Using Cu_2O and $Al(OH)_3$, bulk form of $CuAlO_2$ was synthesized using a conventional solid-state reaction method under vacuum at 1050°C [17]. By melting CuO_x into α-Al_2O_3, the reaction could be provided at 1200°C [18]. The reported process was performed for the first reaction going down to 320–400°C by a mixture of CuCl and $NaAlO_2$ [23]. Generally, complex instrumentations are needed to synthesize $CuAlO_2$. In this presented research, the rapid synthesizing method was used and the influence of defects on the structural, optical, and magnetic properties of $CuAlO_2$ samples was studied. The obtained results were correlated with the results existing in the literature.

2. Material and methods

Direct reaction of chemicals with high purity ($>$ 99% purity) of Cu_2O and Al_2O_3 was subjected to redox reaction (Cu_2O+$Al_2O_3 \rightarrow 2CuAlO_2$). The open-air heat sintering was applied to the resulting sample by increasing the furnace temperature by 4 degrees per min. The final temperature was 1100°C and the sample was kept at this temperature for 1.5 h [24]. The furnace was turned off for self-cooling without the programmed decrease. Structural phases were defined by X-ray diffraction method (Rigaku Multiflex XRD instrument) using a monochromated Cu K_α (1.5418 Å) source in the 2θ scan range of 10–120°. The surface morphology and stoichiometry of the sample were clarified by Jeol-6390-LV Scanning Electron Microscopy (SEM-EDX) tool. To confirm the chemical analysis, X-ray photoelectron spectroscopy (special design) measurement (XPS) was also performed. The field-dependent magnetic behavior (M–H) of the sample and the magnetic moment variation behavior under a temperature range (M–T) were measured by Quantum Design Physical Properties Measurement System (PPMS). The optical properties of the sample were provided in the range of 200–900 nm with the help of the Shimadzu 2600 UV-Spectrophotometer.

3. Results and discussion

3.1. X-ray diffraction (XRD) analysis

The diffraction pattern belonging to the $CuAlO_2$ powder was depicted in Fig. 1.

All peaks in the pattern were indexed and evaluated under the database of ICDD. As can be seen in the evaluated pattern, the contribution of the secondary peak is at a level that can be ignored. The maximum peak formation was observed for (012) at $2\theta = 38.07°$ in Fig. 1, which matches well with the $CuAlO_2$ pattern form in the literature [25]. We found that the indexed peaks belonged to a rhombohedral unit cell with the space group of ($R\bar{3}m$), and the lattice parameters also calculated were $a = 0.2858$ nm and $c = 1.6899$ nm. The secondary peaks of $CuAlO_2$ were marked in Fig. 1 with # and * signs indicating diamagnetic Al_2O_3 and CuO, respectively.

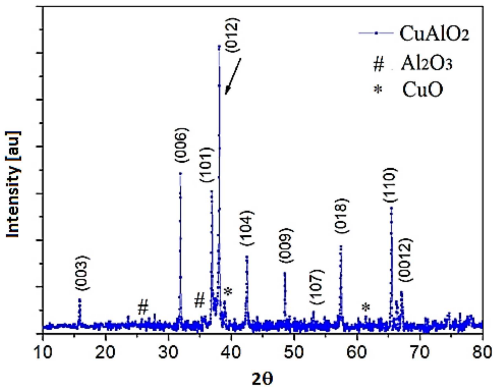

Fig. 1. XRD pattern of $CuAlO_2$ synthesized by solid-state reaction method.

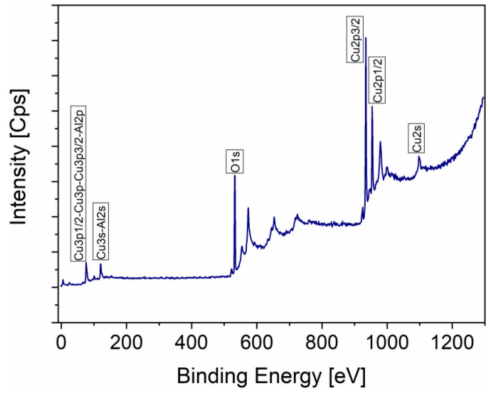

Fig. 2. XPS analysis of $CuAlO_2$ in terms of binding energy.

Using the full width at half maximum (FWHM) of the maximum peak (provided from the ICDD database), the particle size of 40 nm was calculated by using the Debye–Scherrer equation given by

$$D = \frac{K\lambda}{\beta\cos(\theta)}, \tag{1}$$

where β is the intensity at FWHM, θ is the diffraction angle, and K and X-ray wavelength λ constants are 0.9 and 0.15406 nm, respectively.

3.2. X-ray photoelectron spectroscopy (XPS) analysis

Binding energy-dependent XPS analysis of the $CuAlO_2$ sample was demonstrated in Fig. 2 using a wide binding energy range from 0 to 1200 eV.

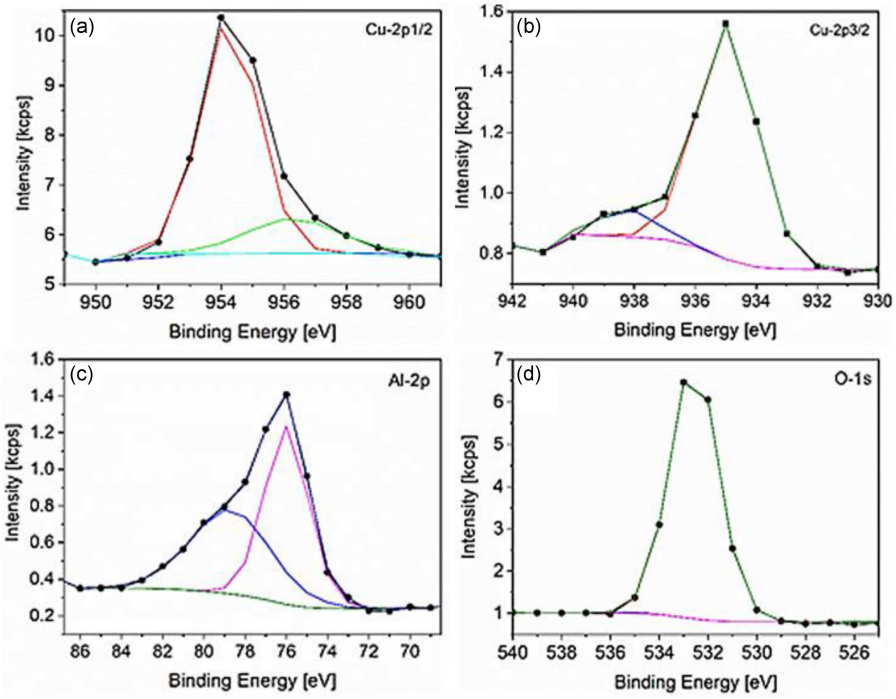

Fig. 3. The core level of XPS spectra (a) Cu $2p1/2$, (b) Cu $2p3/2$, (c) Al $2p$, and (d) O $1s$.

To figure out the chemical compositions of $CuAlO_2$ sample, a detailed XPS measurement was carried out. XPS spectral profiles of core level for the 4 electron-species Cu $2p1/2$, Cu $2p3/2$, Al $2p$, and O $1s$ were depicted in Fig. 3a–d, respectively. The fitted Cu $2p1/2$ deconvolution peak is centered at $\sim$ 954.1 eV (Cu^{2+}) (see Fig. 3a) and similarly seen in [26], and the typical Cu $2p3/2$ peak is located at $\sim$ 934.2 eV (see Fig. 3b), corresponding to Cu^{2+} in the matrix [27]. The XPS studies along with the XRD results indicate that there are two phases ($CuAlO_2$ and Al_2O_3) in our sample [28].

As seen in Fig. 3c, the observed Al $2p$ signal at $\sim$ 75.4 eV is attributed to the existence of Al_2O_3. The typical O $1s$ peak is located at around 533.2 eV in Fig. 3d. It is commonly emphasized in the literature that the O $1s$ core-level spectra with the binding energy values $\sim$ 530 eV and 533.4 eV belong to species with two negative charges, O^{2-}, while the higher intensity peak that reveals at 533 eV is associated with oxygen species including CO_3.

3.3. Scanning electron microscopy (SEM) analysis

The SEM images of the $CuAlO_2$ sample synthesized by the solid-state reaction method of 2 μm magnifications were given in Fig. 4. As seen in Fig. 4, the particles in the images are almost separated from each other and the melting does not become actively effective at the annealing temperature of 1100°C. To evaluate the stoichiometry of the sample, energy dispersive spectroscopy (EDS) measurements were performed from different parts of the sample five times.

TABLE I

The elemental composition details of the $CuAlO_2$ nanopowder.

Element	Weight [%]	Atomic [%]	Net Int. Error
O K series	28.72	53.70	0.01
Al K series	20.02	22.19	0.01
Cu K series	51.26	24.11	0.01

As seen in Fig. 4d, all peaks belong to the $CuAlO_2$ composition and the desired composition, presented in Table I, was achieved. The elemental composition of $CuAlO_2$ with the K shell energy-dependent table was given in Table I. As depicted in Table I, the atomic percentage of $CuAlO_2$ nanopowder is convenient as stoichiometry.

3.4. Photoluminescence (PL) analysis

Photoluminescence (PL) measurements of the $CuAlO_2$ sample were performed in the range of 3.65–1.38 eV by using an excitation wavelength of 300 nm (4.13 eV), see Fig. 5. The two main peaks observed in Fig. 5 are the ultraviolet (UV) emission peak and the broad visible emission band. These peak are responsible for quality of the crystallization and defect numbers in the sample and for the origin of defects, respectively. In addition, a few weak peaks were observed between 3.1 and 2.48 eV.

In the UV region, a sharp transition peak ascribed to near band edge (NBE) transitions was observed at 3.42 eV and 3.29 eV for the $CuAlO_2$

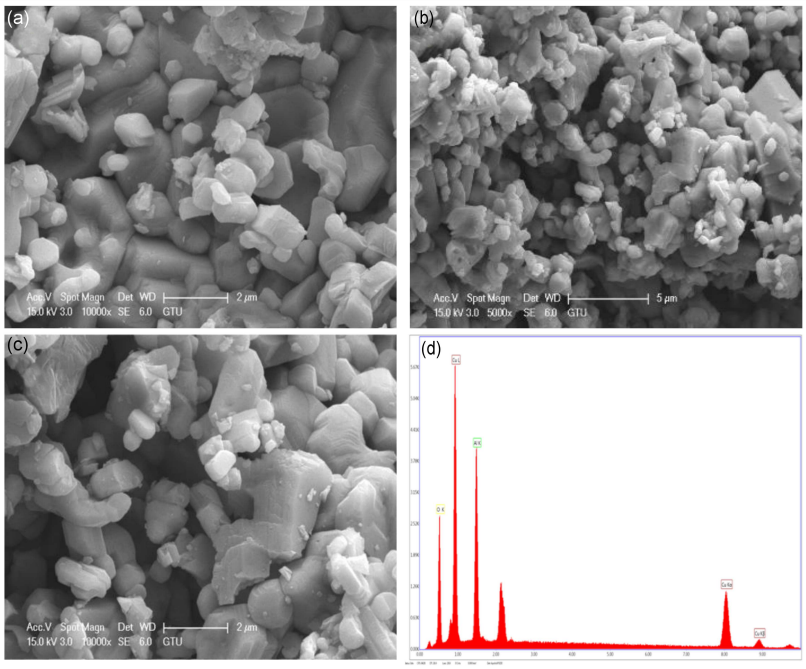

Fig. 4. SEM micro images of the $CuAlO_2$ sample at magnification of (a, b) 2 μm and (c) 5 μm. Panel (d) shows the elemental composition of $CuAlO_2$ sample.

sample. NBE emission is caused by excitonic transitions between electrons and holes, and the stronger the UV emission of the sample, the higher the $c \rightarrow$ crystallization quality and fewer defects occurring. Compared to other studies in the literature, NBE emission appears to have a higher crystallization value. This means that the sample growth annealing temperature is suitable for the quality of the crystallization.

The second dominant and broad emission peak is the visible region known as deep-level (DL) emission, consisting of violet, blue, green, yellow, orange and red emission peaks. Deep-level emission is adjusted impurities or defects such as Cu-interstitial (Cu_i), Cu vacancies (V_{Cu}), Al vacancy (V_{Al}), oxygen vacancies (V_O), and oxygen interstitial (O_i) in the crystal structure. Therefore, the Gaussian decomposition of PL spectra was analyzed by the "Fityk" software.

Nine Gaussian decompositions of PL spectra versus emission wavelength were plotted in Fig. 5. Nine peaks are suited to five emissions; two ultraviolet emissions (Peak 1 and Peak 2) from 3.44 to 3.18 eV can be ascribed to NBE of $CuAlO_2$ as an indication of the excitonic characteristic. One violet emission (Peak 3) from 3.18 to 2.79 eV can be attributed to Cu-interstitial (Cu_i) and two blue emissions (Peak 4 and Peak 5) from 2.79 to 2.52 eV can be attributed to Cu vacancies. In turn, two red emissions (Peak 6 and Peak 7) from 2 to 1.65 eV are consistent with the results of Senol et al. [19].

The red emission is divided into two parts; (2.79–1.80 eV) and (1.80–1.65 eV) can be attributed to the oxygen interstitials (O_i) and the oxygen vacancy (V_O), respectively. Two NIR (near-infrared) emissions (Peak 8 and Peak 9) from 1.65 to 1.61 eV were the results of the oxygen vacancy depicted in [19] (and other references in [19]). Moreover, this can be attributed to the second-order diffraction (a harmonic of the first of the near band-edge) [27].

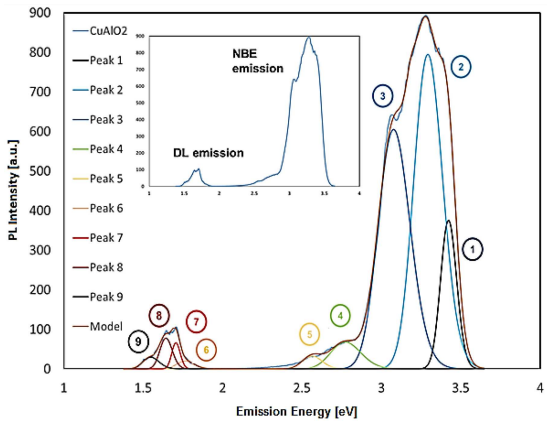

Fig. 5. Gaussian decompositions of PL spectra and inset PL spectra of the $CuAlO_2$ sample.

As seen in Fig. 5, the DL emission (visible region) band consists of the red and NIR emission peaks for the $CuAlO_2$ sample in the wavelength range of 1.77–1.54 eV. It can be concluded that reactions in the solid-state reaction process may cause cooper and oxygen vacancies and affect the luminescence, structural and magnetic properties of the $CuAlO_2$ sample.

3.5. Optical analysis

3.5.1. UV-VIS diffuse reflectance spectra

The bandgap, impurity centers and oxygen deficiency are some of the effective factors that dominate the reflectance properties. As seen in Fig. 6, the synthesized $CuAlO_2$ nanoparticles were optically investigated by wavelength-dependent UV-diffuse reflectance spectroscopy (UV-DRS) in the wavelength range of 330–700 nm. The reflectance of $CuAlO_2$ nanoparticles has a sharp decrease in intensity at wavelength of about 340 nm.

3.5.2. Band gap calculation

The values of the optical band gap E_g depended on several factors such as crystallite size, carrier concentration, lattice strain, and the size effect of the dopant metals in the $CuAlO_2$ lattice. Kubelka–Munk function $F(R)$ was calculated with the use of the diffuse reflectance spectra. It turns out that the optical band gap E_g of the samples can be calculated from the Kubelka–Munk function $F(R)$, which transforms the reflectance (R) data, as given by the relation [28]

$$F(R) = \frac{(1-R)^2}{2R}. \tag{2}$$

The optical band gap (E_g) is typically determined between the absorption coefficient (α) and the photon energy $(h\nu)$ [29] using

$$\alpha h\nu = k\left(h\nu - E_g\right)^{1/n}. \tag{3}$$

In (3), k is the energy-independent constant, and n is a constant depending on the bandgap type, i.e., 1/2 and 2 for the direct and indirect bandgaps, respectively.

Since $F(R)$ is proportional to α, thus for the directly $(n = 1/2)$ and indirectly $(n = 2)$ allowed transitions, (3) can be transformed to

$$\left[F\left(R\right)h\nu\right]^2 = k^2\left(h\nu - E_g\right), \tag{4}$$

and

$$\left[F\left(R\right)h\nu\right]^{1/2} = k^{\frac{1}{2}}\left(h\nu - E_g\right). \tag{5}$$

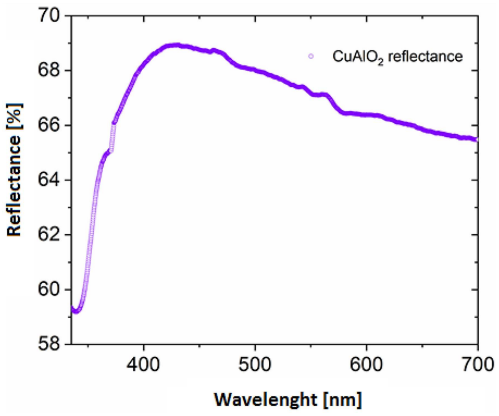

Fig. 6. Reflectance spectra of $CuAlO_2$ sample in the wavelength range from 330 to 700 nm.

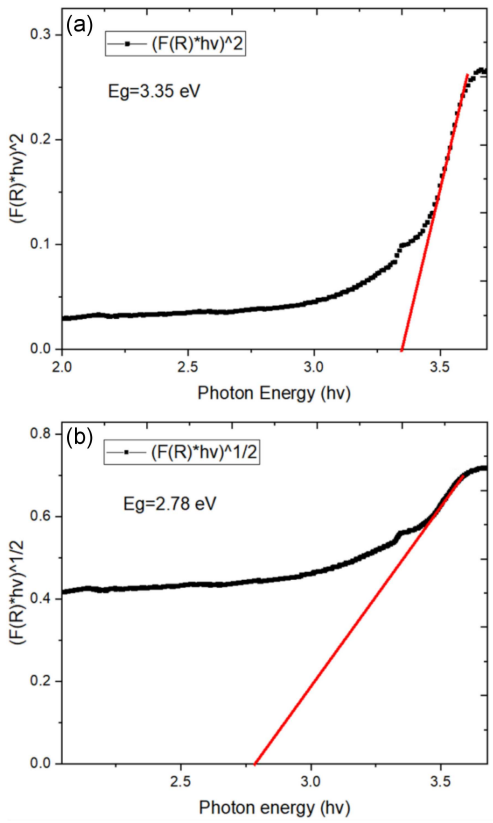

Fig. 7. Plots of (a) $(F(R)h\nu)^2$, (b) $(F(R)h\nu)^{1/2}$ as a function of photon energy $(h\nu)$ for the $CuAlO_2$ nanoparticles.

TABLE II

Calculatiion of the direct and indirect bandgap energies for the $CuAlO_2$ nanoparticles.

Bandgaps	I [eV]
$E_{g-\mathrm{direct}}$	3.35
$E_{g-\mathrm{indirect}}$	2.78

As shown in Table II and Fig. 7, the direct and indirect bandgap energies (denoted E_g-direct and E_g-indirect) were calculated by the linear approximation of the graphical slopes of $(F(R)h\nu)^2$ and $(F(R)h\nu)^{1/2}$ to the photon energy axis, where $F(R) = 0$. In other words, the value of E_g was obtained from the intersection between the linear fit and the photon energy axis. As shown in Fig. 7, the direct and indirect bandgap energies of the $CuAlO_2$ nanoparticles samples were observed as 3.35 eV and 2.78 eV, respectively. The obtained values were compatible both with the experimental and theoretical values in the literature [30–33].

3.6. Magnetic analysis

Figure 8 shows the magnetization curves of $CuAlO_2$ prepared at 1100°C. At low and high temperatures, weakly nonlinear magnetization curves

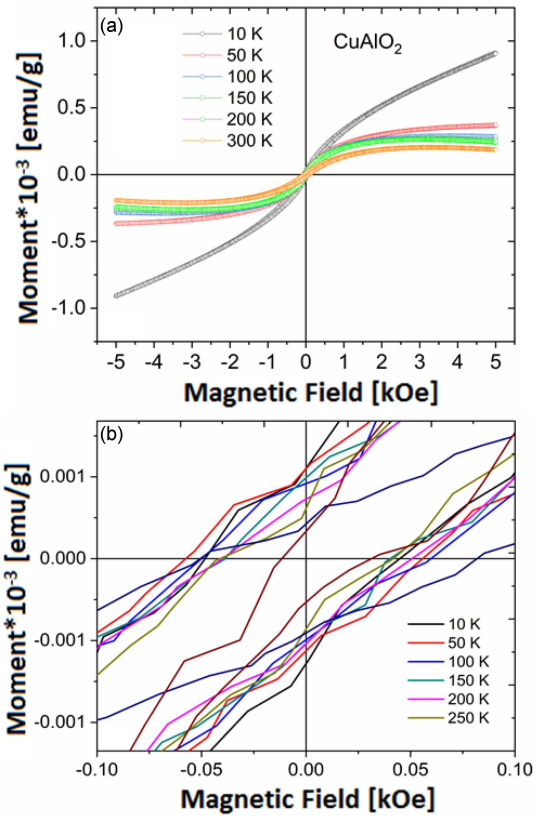

Fig. 8. (a) Isothermal $M(H)$ loops (at 0.5 T) of $CuAlO_2$ nanoparticles were measured at six different temperatures. The H_c coercive field variations were depicted in panel (b).

were observed due to the presence of the ferromagnetic-like contribution. In all measured temperatures, the magnetic parameters on hysteresis curves were presented in Table III. In Fig. 8 it is seen that a sudden drop and a transition to lower moment values were observed between 10 and 50 K in the $CuAlO_2$ sample, so we conclude that this is an indication of dominant thermal magnetization in the sample. A decrement was also observed in the M–H curve and the result of steady increase of the measurement temperature gradually up to 300 K. As a result of residual CuO, low-temperature paramagnetism in $CuAlO_2$ was reported by Tate et al. [34]. In fact, the Cu^{2+} ion was also observed in our sample. The paramagnetic nature of the $CuAlO_2$ sample should be also explained by the presence of Cu^{2+} with the d^9 electronic configuration. The electron holes accounting for the divalent Cu^{2+} ions move in a valence band for conduction [2]. Additionally, the role of impurity and residual ferromagnetic contributions is still a matter of discussion. As seen in Pauli's paramagnetism, there should be spin and orbital motions of the delocalized electrons in this sample. The coercivity (H_c) and the remanent magnetization (M_r) values were directly provided from the M vs H dependence in Fig. 8a and b.

TABLE III

The remanent magnetization, saturation magnetization, and coercivity field in all measured temperatures of the $CuAlO_2$ sample.

Constant measuring temp. [K] for M vs H	Remanent magnetisation M_r [emu/g]	Saturation magnetisation M_s [emu/g]	Coercivity field H_c [Oe]
10	2.222×10^{-5}	–	
50	2.194×10^{-5}	3.728×10^{-4}	1.715
100	1.838×10^{-5}	2.886×10^{-4}	14.525
150	1.948×10^{-5}	2.461×10^{-4}	5.059
200	1.426×10^{-5}	2.344×10^{-4}	4.465
300	0.834×10^{-5}	1.924×10^{-4}	14.595

As seen in Fig. 8b, the magnetization value exhibits an increment with the external magnetic field in the low field region. However, even in the presence of a relatively strong magnetic field at 6 kOe, magnetization does not reach the saturation level. The ferromagnetic feature of $CuAlO_2$ should be associated with Cu^{2+}, which is structurally paramagnetic.

The ferromagnetic feature of $CuAlO_2$ should be associated by Cu^{2+}, which is structural paramagnetic. To figure out the ferromagnetic properties of $CuAlO_2$, the following equations were fitted

$$M = M_0 + \chi H + M_s B_j(T, H), \tag{6}$$

$$B_j(T,H) = \frac{2J+1}{2J} \coth\left(\frac{2J+1}{2J}x\right) - \coth\left(\frac{x}{2J}\right). \tag{7}$$

Here B and J are the Brillouin function and the total moment, respectively.

The blue colored data in Fig. 9 represent the M-H measurement at 10 K and the line given by orange color belongs to the fitted Brillouin curve. The magnetization curve at 10 K was fitted by the M-Brillouin model (see (6) and (7)). The optimized fitting parameters, M_s, M_0, μ_H, χ, and J were calculated as 5.35×10^{-5} emu/g, 2.741×10^{-7} emu/g, 30 μ_B/f.u, 1.20×10^{-7} emu/gOe, and 0.1, respectively. In (7), x parameter is equal to $x = \mu_H H/(k_B T)$ where k_B is the Boltzmann constant and μ_H in x parameter is $\mu_H = gJ\mu_B$ in which g is the Land'e g-factor, J is the total moment, and μ_B is the Bohr magnetron. Figure 9 manifests the trace of the ferromagnetic contribution due to either the role of impurity or the residual ferromagnetic contributions. No saturation was observed with the applied magnetic field $H = \pm 6$ kOe. The overall behavior is a typical paramagnetic behavior, and the reason for this is addressed to Cu^{2+} with the d^9 electronic configuration in the structure [29].

Figure 10 manifests the magnetization vs temperature curves of the $CuAlO_2$ sample taken under the field-cooled (FC) condition through a 5 kOe field. The M vs T data was fitted to the Curie-Weiss law and the parameters were calculated by fitting.

TABLE IV

The peak center, height, area, FWHM values, emission range, and origin of PL emission of the $CuAlO_2$ sample.

Peak label	Center [nm]	Center [eV]	Height	Area	FWHM	Emission range	Origin	
Peak 1	362.344	3.42	376.029	5032.28	12.5722	ultraviolet	excitons	NBE emis.
Peak 2	376.651	3.29	794.57	20597.6	24.353	ultraviolet	excitons	
Peak 3	403.064	3.08	605.38	19852.7	30.8077	violet	Cu-interstitial	DL emission
Peak 4	447.402	2.77	68.5502	2616.25	35.854	blue	V_{Cu}	
Peak 5	483.93	2.56	32.8344	961.749	27.5169	blue	V_{Cu}	
Peak 6	703.04	1.76	20.3157	1096.88	50.722	red	V_O	
Peak 7	727.04	1.71	66.743	1893.04	26.6454	red	V_O	
Peak 8	755	1.64	78.436	3511.81	42.0613	NIR (near-infrared)	V_O	
Peak 9	801.9	1.55	29.6535	1955.68	61.9569	NIR (near-infrared)	V_O	

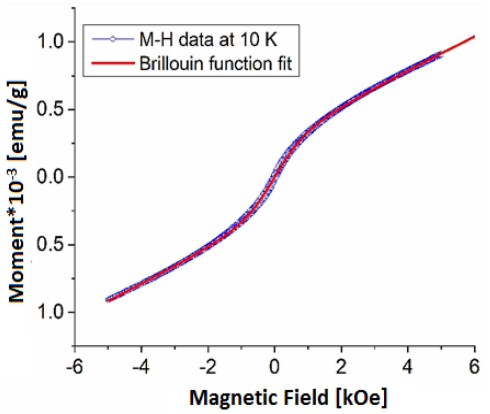

Fig. 9. The magnetic moment M as a function of the field H in the range from -6 to 6 kOe, measured at 10 K for the $CuAlO_2$ sample.

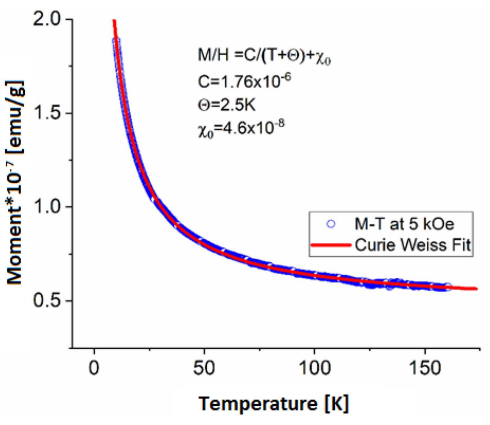

Fig. 10. Temperature-dependent magnetization curve with Curie–Weiss fitting.

The obtained values related to the Curie-Weiss law were exhibited in Fig. 10. Using the presented FC data from 10 to 150 K, the Currie–Weiss temperature of 1.4 K was obtained [34]. It is known in the literature that the $CuAlO_2$ magnetic behavior should

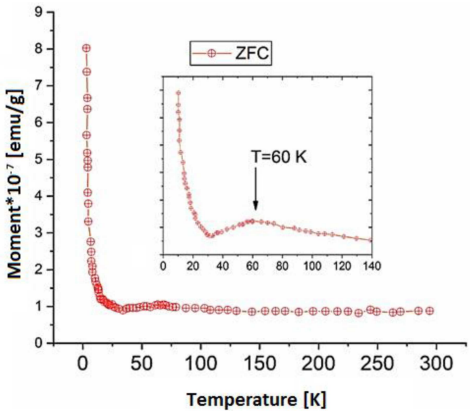

Fig. 11. Temperature-dependent ZFC magnetization curve showing antiferromagnetic behavior.

be diamagnetic due to Cu^+, Al^{3+}, and O^{2-} possessing unpaired electrons and preparing a highly pure and stoichiometric $CuAlO_2$ is a very difficult task. So far, in bulk, diamagnetism has not been supported for the $CuAlO_2$ matrix due to p-type conduction [34–36].

In Fig. 11, the temperature-dependent magnetization behavior of the $CuAlO_2$ sample in the zero-field cooling (ZFC) case was presented in the temperature range from 0 to 300 K. As seen in the inset curve, especially at 60 K, an antiferromagnetic short-range-order has been developed. The reason for this could be the preparation method which causes oxygen vacancies, especially in the case of the solid-state reaction method. The antiferromagnetic short-range-order revealed at 60 K in the inset in Fig. 11 is ascribed to the mixed state of Cu^{2+} and Cu^+ with a high amount of oxygen vacancies in the Cu–O sub-lattice. The existence of oxygen vacancies was also revealed in the PL measurements in Fig. 5. As seen in the Gaussian decompositions of PL spectra, the red emission part was divided into two parts, attributed to oxygen interstitials (O_i) and oxygen vacancy (V_O) (please see Table IV

for further details on the related wavelengths). The existence of O 1*s* was also provided by the XPS results. Hence, we conclude that the magnetic properties of the $CuAlO_2$ system were affected by oxygen vacancies, which are mainly the result of the conditions and methods of preparation.

4. Conclusions

A direct reaction of chemicals was subjected to a redox reaction ($Cu_2O+Al_2O_3 \rightarrow 2CuAlO_2$) to obtain the final composition of $CuAlO_2$. The desired crystalline phase was achieved and all peaks in the XRD phase investigation were found to belong to the $CuAlO_2$ pattern. The particle size was calculated to be about 40 nm. XPS measurements proved that the core level of the 4 electron species Cu 2*p*1/2, Cu 2*p*3/2, Al 2*p*, and O 1*s* exists. The direct and indirect band gaps of the $CuAlO_2$ composition were determined as 3.35 eV and 2.78 eV, respectively. The results of fitting of XPS in Fig. 3a revealed that especially the Cu 2*p*1/2 deconvolution peak centered at $\sim$ 954.1 eV belongs to Cu^{2+}, and this fact was the indication of the paramagnetic behavior of the material. In addition, the role of impurity and residual ferromagnetic contributions may be possible in $CuAlO_2$ due to exhibiting a trace of ferromagnetic behavior. The related parameters were presented in Table I. The magnetic field-dependent magnetization curve at 10 K was fitted by a M-Brillouin model and showed the dominant paramagnetic contribution. No diamagnetic contribution was detected in our sample. Using the nonlinear behavior of the temperature-dependent FC magnetization, the Curie temperature was calculated as 1.4 K. It was done by fitting the data to Curie–Weiss expression, as shown Fig. 10. The paramagnetic nature of the sample was provided in both detailed XPS and magnetic measurements. The ZFC curve manifested that the concavity at $\sim$ 60 K was due to an antiferromagnetic short-range order and this effect is the reason for oxygen vacancies revealed in the XPS and PL results.

Acknowledgments

We thank Prof. Yildirhan Oner for his useful discussion and Dr. Dimitry Shulgin for sample preparation. This work was supported by the Research Fund of Bahcesehir University (Project No: BAP-2021.01.27 and BAP.2019-01.04).

References

[1] H. Ohta, K. Nomura, H. Hiramatsu, K. Ueda, T. Kamiya, M. Hirano, H. Hosono, *Solid State Electron.* **47**, 2261 (2003).

[2] V.L. Matukhin, I.H. Khabibullin, D.A. Shulgin, S.V. Schmidt, E.I. Terukov, *Semiconductors* **46**, 1102 (2012).

[3] H. Kawazoe, M. Yasukawa, H. Hyodo, M. Kurita, H. Yanagi, H. Hosono, *Nature* **389**, 939 (1997).

[4] T. Ishiguro, A. Kitazawa, N. Mizutani, M.J. Kato, *J. Solid State Chem.* **40**, 170 (1981).

[5] L. Dloczik, Y. Tomm, R. Könenkamp, M.C. Lux-Steiner, T. Dittrich, *Thin Solid Films* **451–452**, 116 (2004).

[6] A.N. Banerjee, S. Kundoo, K.K. Chattopadhyay, *Thin Solid Films* **440**, 5 (2003).

[7] A.N. Banerjee, K.K. Chattopadhyay, *J. Appl. Phys.* **97**, 084308 (2005).

[8] B.J. Ingram, T.O. Mason, R. Asahi, K.T. Park, A.J. Freeman, *Phys. Rev.* **64**, 155114 (2001).

[9] A.N. Banerjee, R. Maity, K.K. Chattopadhyay, *Mater. Lett.* **58**, 10 (2003).

[10] C.H. Ong, H. Gong, *Thin Solid Films* **445**, 299 (2003).

[11] H. Gong, Y. Wang, Y. Luo, *Appl. Phys. Lett.* **76**, 3959 (2000).

[12] H. Katayama-Yoshida, T. Koyanagi, H. Funashima, H. Harima, A. Yanase, *Solid State Commun.* **126**, 135 (2003).

[13] H. Yanagi, S. Inoue, K. Ueda, H. Kawazoe, H. Hosono, N. Hamada, *J. Appl. Phys.* **88**, 4159 (2000).

[14] M.S. Lee, T.Y. Kim, D. Kim, *Appl. Phys. Lett.* **79**, 2028 (2001).

[15] K. Tonooka, K. Shimokawa, O. Nishimura, *Thin Solid Films* **411**, 129 (2002).

[16] X.G. Zheng, K. Taniguchi, A. Takahashi, Y. Liu, C.N. Xu, *Appl. Phys. Lett.* **85**, 1728 (2004).

[17] V.H. Hahn, C.D. Loreht, *Anorg. Allg. Chem.* **279**, 281e288 (1955).

[18] E.J. Gonzales, K.V. Trumble, *J. Am. Ceram. Soc.* **79**, 114 (1996).

[19] S.D. Senol, E. Ozugurlu, L. Arda, *J. Alloys Compd.* **822**, 153514 (2020).

[20] M. Tosun, L. Arda, *Ceram. Int.* **45**, 16234 (2019).

[21] L. Arda, *J. Magn. Magn. Mater.* **475**, 493 (2019).

[22] A. Guler, L. Arda, N. Dogan, C. Boyraz, E. Ozugurlu, *Cer. Int.* **45**, 1737 (2019).

[23] D. Xiong, X. Zeng, W. Zhang, H. Wang, X. Zhao, W. Chen, Y.-B. Che, *Inorg. Chem.* **53**, 4106 (2014).

[24] F.A. Benko, F.P. Koff-Yberg, *J. Phys. Chem. Solids* **45**, 57 (1984).

[25] N. Benreguia, B. Bellal, M. Trari, *J. Hazard. Mater.* **192**, 1395 (2011).

[26] S. Liu, Z. Wu, Y. Zhang, Z. Yao, J. Fan, Y. Zhang, J. Hu, P. Zhang, G. Shao, *Phys. Chem. Chem. Phys.* **17**, 557 (2015).

[27] M. Aziziha, S.A. Byard, R. Beesely, J.P. Lewis, M.S. Seehra, M.B. Johnson, *AIP Adv.* **9**, 035030 (2019).

[28] P. Kubelka, F. Munk, *Z. Tech. Phys.* **12**, 593 (1931).

[29] S.M. Sze, *Physics of Semiconductor Devices*, J. Wiley & Sons, 1969, p. 52.

[30] A.S. Shamshirgar, M. Aghayan, T.S. Tripathi, M. Karppinen, M. Gasik, I. Hussainova, *Mater. Design* **147**, 48 (2018).

[31] M. Fang, H. He, B. Lu, W. Zhang, Z. Zhao, J. Huang, *Appl. Surf. Sci.* **257**, 8330 (2011).

[32] J. Pellicer-Porres, A. Segura, A.S. Gilliland, A. Muñoz, P. Rodríguez-Hernández, D. Kim, M.S. Lee, T.Y. Kim, *Appl. Phys. Lett.* **88**, 181904 (2006).

[33] F. Min, B. Haiping, H. Lu, Z. Weiguang, Z. Binghui, Y. Zhizhen, H. Jingyun, *Appl. Surf. Sci.* **257**, 8330 (2011).

[34] J. Tate, H.L. Ju, J.C. Moon, A. Zakutayev, A.P. Richard, J. Russell, D.H. McIntyre, *Phys. Rev. B* **80**, 165206 (2009).

[35] J. Christopher, C.S. Swamy, *J. Mol. Catal.* **21**, 745e752 (1986).

[36] M. Senna, P. Bllik, A.Y. Yermakov, M. Skratek, M. Majerova Caplovicova, M. Micusik, L. Caplovic, M. Bujdos, M. Nosko, *J. Alloys Compd.* **695**, 2314e2323 (2017).